Ceramics International xxx (xxxx) xxx

Contents lists available at ScienceDirect

Ceramics International

journal homepage: www.elsevier.com/locate/ceramint

$BaMnV_2O_7$: A novel microwave dielectric ceramic for LTCC applications

Houlin Hu [a], Yao Wang [b], Chaoyang Cai [a], Pengcheng Zhang [a], Xiaoqing Chen [a], Rui Xiang [a], Hao Li [a,*]

[a] College of Electrical and Information Engineering, Hunan University, Changsha, 410082, China
[b] China Architecture Design & Research Group, Beijing, 100120, China

ARTICLE INFO

Keywords:
Microwave dielectric properties
$BaMnV_2O_7$
LTCC

ABSTRACT

A novel low-temperature fired $BaMnV_2O_7$ ceramic was fabricated with solid-state reaction. Rietveld refinements based on X-ray diffraction data and TEM analysis indicated that $BaMnV_2O_7$ exhibited a monoclinic structure with a P21/n space group. The dense microstructure of the $BaMnV_2O_7$ ceramic obtained at 850 °C was examined by scanning electron microscopy. The increasing content of V^{4+} affected the quality factor, which was confirmed by X-ray photoelectron spectroscopy. The intrinsic dielectric properties were obtained from far infrared reflectivity spectra. Additionally, the $BaMnV_2O_7$ ceramic showed good chemical stability with a Ag electrode and desirable microwave dielectric performance at 850 °C: $\epsilon_r = 11.7$, $Q \times f$ =20040 GHz and $\tau_f = -48.2$ ppm/°C, which can potentially be applied in LTCC technology.

1. Introduction

W ith the recent revolution in wireless communication, 5th-generation communication technology has been widely applied in different fields. Microwave dielectric ceramics play a significant role in terms of improving the transmission efficiency of communication systems [1–4]. For industrial applications, microwave dielectric ceramics need to possess an appropriate permittivity (ϵ_r), a high quality factor ($Q \times f$) and a near-zero temperature coefficient (τ_f) [5–7]. Low-temperature co-fired ceramic (LTCC) is becoming the current research hotspot due to the development of advanced passive integrated and hybrid circuit packaging technology [8–10]. In addition, LTCC requires dielectric ceramics to have no chemical reaction with inner electrodes during the co-fired process and possess a low sintering temperature.

To date, there have been a considerable number of low-firing ceramics with excellent dielectric properties, such as vanadates, tungstates, molybdates, tellurates and borates [11]. Among them, vanadates have been widely investigated for LTCC applications because V_2O_5 possesses a low melting point (690 °C), such as $BiVO_4$ [12], $SrZnV_2O_7$ [13], $0.45BiVO_4$-$0.55TiO_2$ [14], $BaTa_2V_2O_{11}$ [15], and $LiCa_3ZnV_3O_{12}$ [16]. Joung et al. reported the dielectric performances of $R_2V_2O_7$ (R = Ba, Sr and Ca) ceramics sintered at 950 °C: ϵ_r = 10.1–12.1, $Q \times f$ = 15200–51630 GHz and $\tau_f = -26.5 \sim +34.8$ ppm/°C [17]. In addition, $BaMV_2O_7$ (M = Mg, Zn and Ca) ceramics were found to possess promising microwave dielectric performances: ϵ_r = 8.2–10.7, $Q \times f$ = 31000–37600 GHz and $\tau_f = -35.2 \sim +64.4$ ppm/°C with low sintering temperatures (<960 °C) [18,19]. Considering that the $BaZnV_2O_7$ ceramic possesses good dielectric properties and that the radius of Mn^{2+} (r = 0.75 Å) is close to that of Zn^{2+} (r = 0.68 Å), it is worthwhile to explore the dielectronic properties of $BaMnV_2O_7$ ceramics.

In this paper, the synthesis technology, crystal structure and microwave dielectric performances of $BaMnV_2O_7$ ceramic were investigated systematically. The far infrared spectrum was applied to identify intrinsic dielectric loss of samples. In addition, $BaMnV_2O_7$ ceramic co-fired with silver for LTCC application was studied in detail.

2. Experimental procedure

The $BaMnV_2O_7$ ceramic was prepared via a traditional solid-state reaction, in which high purity $BaCO_3$ (99.8%, Aladdin, China), $MnCO_3$ (99.95%, Aladdin, China) and NH_4VO_3 (99%, Aladdin, China) were first weighed according to stoichiometry. The preparative powders were mixed with zirconia balls and an alcohol mill for 6 h, and the mass ratio of different zirconium balls is 1:1. And then the mixtures were calcined at 750 °C for 4 h, re-milled, and dried. Afterwards, 10 wt% polyvinyl alcohol binder was mixed with the powders and ground until the powders were granulated. After the powders were pressed in the grinding tool at 20 MPa, the cylinder was sintered at 810–870 °C for 4 h.

The Archimedes method was applied to measure the density of the ceramics. Room temperature X-ray diffraction (XRD) was applied to

* Corresponding author.
E-mail address: hli@hnu.edu.cn (H. Li).

https://doi.org/10.1016/j.ceramint.2021.08.028
Received 9 June 2021; Received in revised form 18 July 2021; Accepted 3 August 2021
Available online 4 August 2021

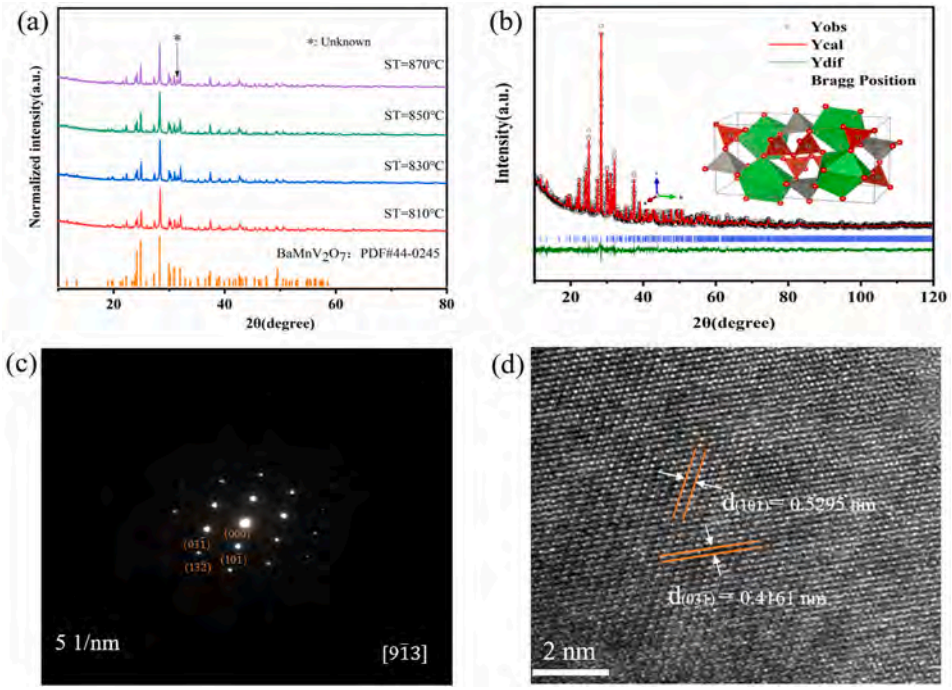

Fig. 1. (a) The XRD patterns of $BaMnV_2O_7$ ceramics sintered at 810–870 °C.
(b) The refined pattern of $BaMnV_2O_7$ ceramic sintered at 850 °C.
(c) The SAED patterns of $BaMnV_2O_7$.
(d) The HRTEM image of $BaMnV_2O_7$ along [9$\bar{1}$3] zone axis.

Table 1
Structure parameter of $BaMnV_2O_7$ ceramics with different sintering temperatures.

S.T.(°C)	a(Å)	b(Å)	c(Å)	α (°)	*β* (°)	*γ* (°)	*Rp* (%)	*Rwp* (%)	*χ2*
810	5.6209	15.2694	7.3959	90	95.591	90	4.56	5.98	1.713
830	5.6190	15.2657	7.3940	90	95.586	90	4.18	5.39	1.449
850	5.6181	15.2661	7.3926	90	95.587	90	4.15	5.39	1.503
870	5.6190	15.2669	7.3927	90	95.591	90	4.17	5.39	1.507

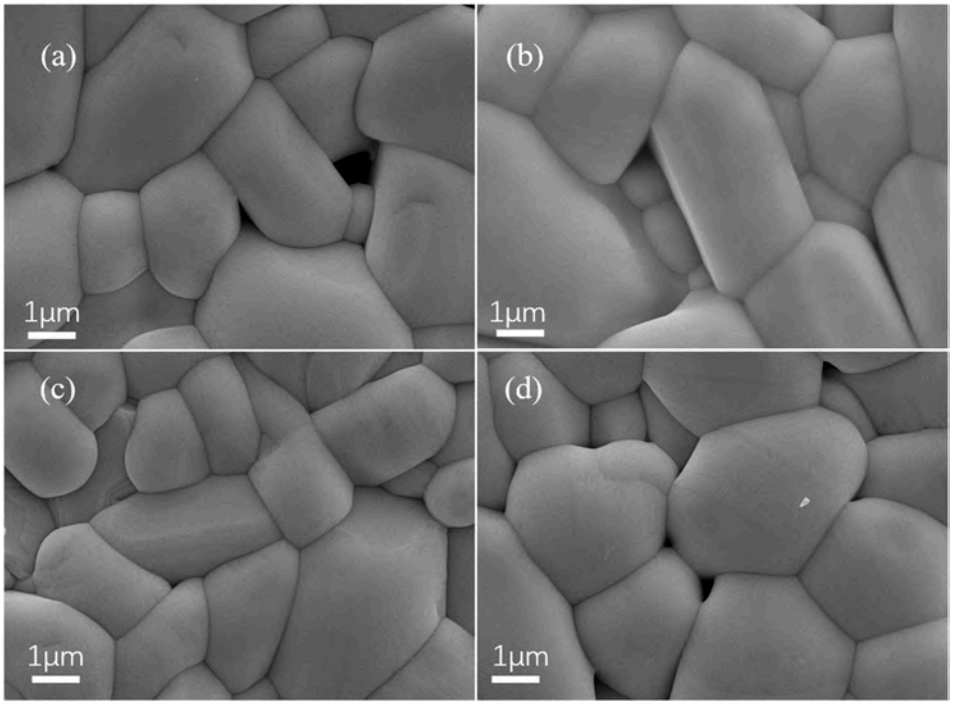

Fig. 2. The SEM micrographs of $BaMnV_2O_7$ ceramics sintered at different temperature, where parts (a–d) are 810, 830, 850 and 870 °C, respectively.

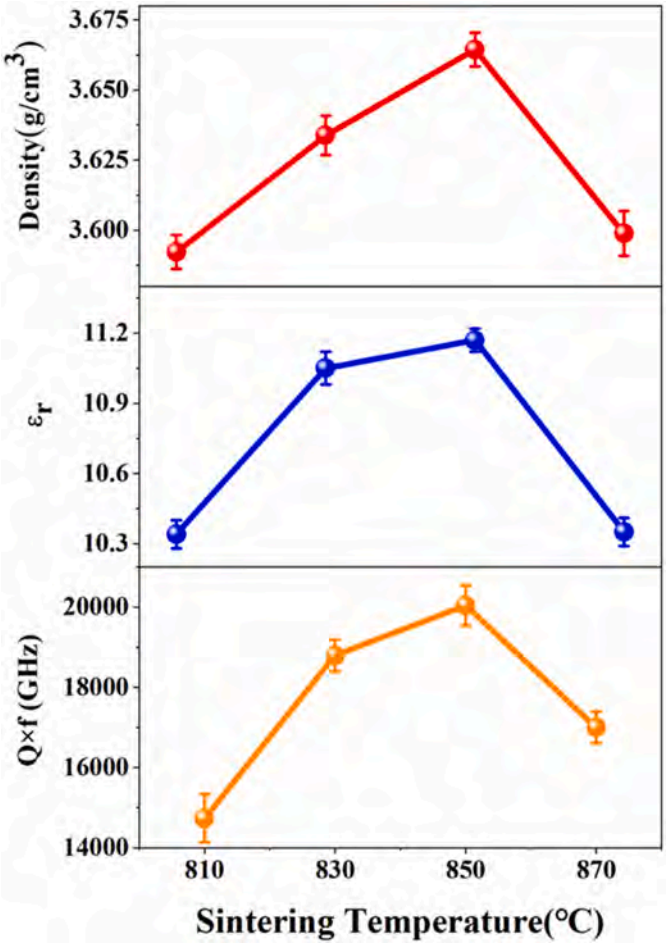

Fig. 3. The variation of (a) bulk density, (b) ε_r and (c) Q × f of $BaMnV_2O_7$ ceramics.

determine the crystalline phase. Rietveld refinement was used to calculate the lattice parameters by GSAS-EXPGUI software [20]. To further confirm the structure of the sintered samples, high-resolution transmission electron microscopy (HRTEM) and selected area electron diffraction (SAED) were conducted. The microstructure of $BaMnV_2O_7$ ceramics at different temperatures was observed by scanning electron microscopy. The valence of sintered samples was measured with X-ray photoelectron spectroscopy (XPS). The τ_f value was determined by resonant frequencies as follows:

$$\tau_f = \frac{f_{85} - f_{25}}{f_{25}(85-25)} \times 10^6 (ppm/^\circ C) \quad (1)$$

where resonant frequencies f_{85} and f_{25} were measured at 85 °C and 25 °C, respectively.

3. Results and discussion

Fig. 1(a) exhibits the XRD patterns of $BaMnV_2O_7$ ceramics sintered at 810–870 °C for 4 h. The observed peaks were indexed to the phase $BaMnV_2O_7$ (PDF#44-0245) with the P21/n space group, but few unknown second phases existed. Fig. 1(b) shows the Rietveld refinement pattern of the $BaMnV_2O_7$ ceramic sintered at 850 °C. The lattice parameters from refinement were a = 5.6181 Å, b = 15.2661 Å, c = 7.3926 Å, α = γ = 90° and β = 95.587°. The values of R_p, R_{wp} and $\chi 2$ at different temperatures are summarized in Table 1, which verified the validity of the refinement results. In addition, the crystal structure of $BaMnV_2O_7$ is exhibited in the inset of Fig. 1(b). $BaMnV_2O_7$ contains two

Table 2
Bulk density and relative density of $BaMnV_2O_7$ ceramics with different sintering temperatures.

S.T.(°C)	Bulk Density(g/cm^3)	Relative Density(%)
810	3.5922	89.81
830	3.6338	90.85
850	3.6644	91.61
870	3.5988	89.97

V atoms, featuring corner-shared VO_4 tetrahedra. Ba^{2+} and Mn^{2+} show eight coordinations and five coordinations with oxygen, respectively.

Fig. 1(c),(d) represents the SAED and HRTEM images based on transmission electron microscopy analysis, which further confirms the structure of $BaMnV_2O_7$. The SAED pattern of $BaMnV_2O_7$ along the $[9\bar{1}3]$ zone axis and the corresponding HRTEM image are displayed. The HRTEM image exhibited interplanar spacings of 0.5295 nm and 0.4161 nm, which were consistent with the $(10\bar{1})$ and $(03\bar{1})$ lattice planes of the $BaMnV_2O_7$ ceramic. Thus, the TEM analysis corresponded to the XRD data, which indicated that the $BaMnV_2O_7$ ceramic crystallized in the monoclinic space group P21/n.

Fig. 2(a)-(d) show the SEM images of the $BaMnV_2O_7$ ceramic sintered at 810°C–870 °C for 4 h. As observed from Fig. 2(a), small grains and pores existed. With the increase in sintering temperature to 850 °C (Fig. 2(c)), pores gradually decreased, and the grain size became uniform, presenting a dense microstructure. However, excessive temperature caused the microstructure to exhibit abnormal grain growth and an uneven grain size (Fig. 2(d)), which generated negative impacts on the dielectric properties.

Fig. 3(a) reveals the relationship between the bulk density and permittivity of the $BaMnV_2O_7$ ceramic and the relative density of $BaMnV_2O_7$ were showed in Table 2. The density increased with temperature throughout the sintering process and reached a maximum at 850 °C. However, once the sintering temperature reached 870 °C, the bulk density began to decline slightly, which was consistent with the change in microstructure. Meanwhile, both dielectric constant and bulk density possessed a similar trend and the highest dielectric constant of 11.17 was obtained when the ceramics were the densest(Fig. 3(b)), which indicated that the density was a significant factor affecting the dielectric constant.

Considering the strong relevance between the observed dielectric constant and the bulk density, it is necessary to discuss the dielectric constant in terms of porosity [21]. Therefore, the influence of pores on ε_r was described by spherical pore models as follows [22]:

$$\varepsilon_r = \varepsilon_{rc}\left(1 - \frac{3P(\varepsilon_{rc}-1)}{2\varepsilon_{rc}+1}\right) \quad (2)$$

where ε_{rc} is the porosity corrected ε_r, and P is the fractional porosity.The values of ε_{rc} are slightly higher than the values of ε_r, suggesting pores existed as a negative factor causing a decrease variation of dielectric constant in $BaMnV_2O_7$ ceramic. Similar results were reported at $BaZnP_2O_7$ ceramic [23]. Generally, the factors affecting the Q × f value are divided into two aspects: internal factors containing the interaction with phonons and external factors such as dislocation, pores and grain size [24]. As observed from Fig. 3(c), the variation in the Q × f value had a similar trend with porosity during the process of sintering. Therefore, the effect of density on the Q × f value is critical.

Moreover, the volatilization of V_2O_5 at high sintering temperatures might result in a decrease in the Q × f value in vanadium ceramics. Similar experimental results were reported in $Ca_5Co_4(VO_4)_6$ and $BaMgV_2O_8$ ceramics [25,26]. Therefore, XPS analysis was implemented to confirm the valence state of vanadium in the $BaMnV_2O_7$ ceramic. Fig. 4 shows the curves of the V 2p region of $BaMnV_2O_7$ ceramic at 810°C–870 °C based on the fitting of Gaussian-Lorentzian curve. The results suggested that the peak of V $2p_{3/2}$ contained V^{4+} and V^{5+}, The positions of V $2p_{3/2}$ with different temperatures were 516.4, 516.5,

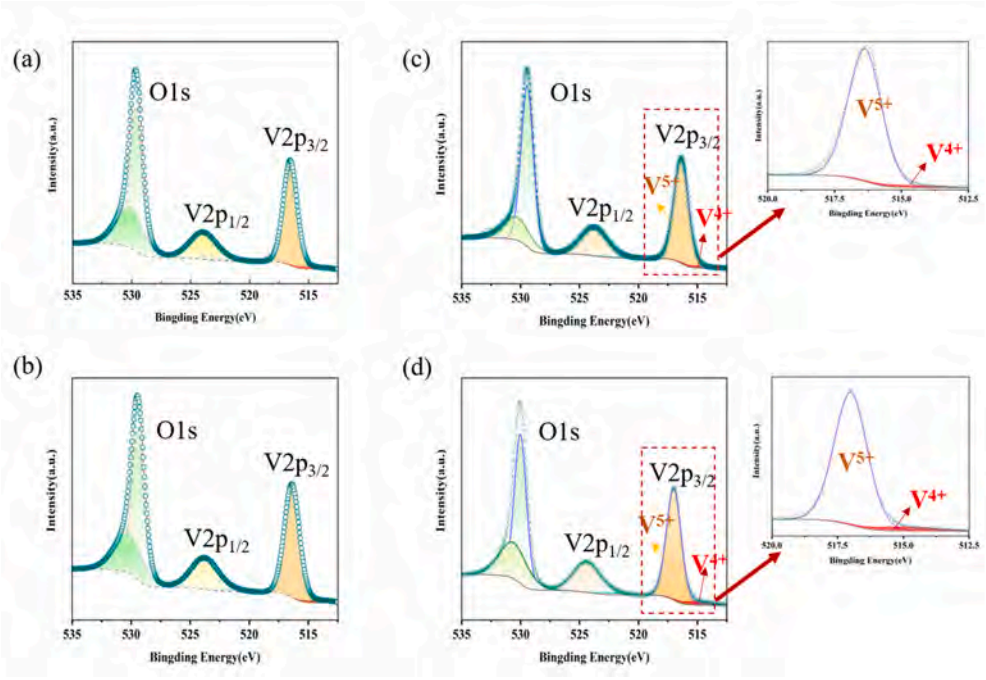

Fig. 4. The relationship between bond valence and temperature coefficient of resonant frequency.

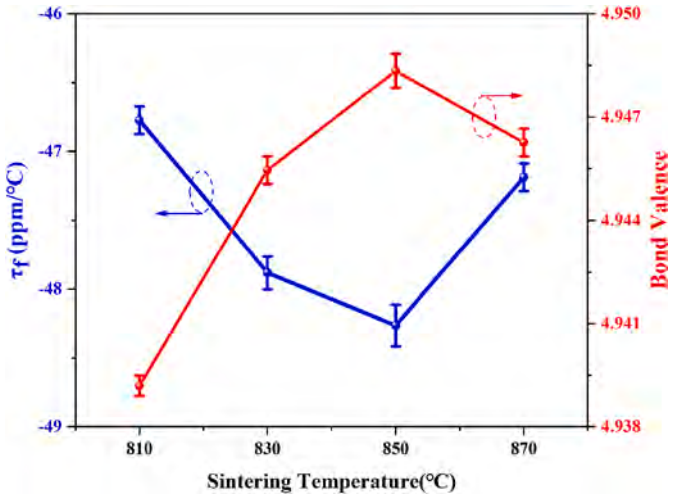

Fig. 5. XPS spectra of V 2p region in $BaMnV_2O_7$ sintered at (a) 850 °C and (b) 870 °C.

515.2 and 516.9 eV, respectively, which were consistent with previous research [27]. As shown in Fig. 4(b), the V^{4+} content was the lowest at 850 °C with a value of 1.09%. However, as the sintering temperature increased to 870 °C (Fig. 4(d)), the V^{4+} content increased to 1.88%. Therefore, the content of V^{4+} in the whole sintering process is low and the content variation is not obvious.

In addition, the thermal stability of ceramics is described by the temperature coefficient. In the $La_2(Zr_{1-x}Ti_x)_3(MoO_4)_9$ system, the increase in bond energy indicated that the system tended to stabilize [28]. Lim et al. revealed a close relationship between octahedral distortion and bond valence [29]. Considering the change in V ion bond valence from the XPS analysis, it is necessary to evaluate the effect of V-O on τ_f. The bond valences are calculated according to the following equations [30,31]:

$$V_i = \sum_j V_{ij} \tag{3}$$

$$V_{ij} = e^{\frac{R_{ij}-d_{ij}}{b}} \tag{4}$$

where R_{ij} represents the bond valence parameter, d_{ij} represents the length of the bond between the cation and anion, and b equals 0.37 Å [32]. As exhibited in Fig. 5, the bond valence gradually increases until 850 °C and begins to decrease at 870 °C, indicating that low bond valence leads to a decrease in energy for recovering the structure. τ_f had an opposite trend with the bond valence of V-O, suggesting that the larger τ_f value of $BaMnV_2O_7$ was associated with the smaller bond valence, and the variation of the τ_f value was affected by the bond valence of V-O.

Dielectric loss is composed of intrinsic and extrinsic loss, lattice vibration is the main influence factor on the variation of intrinsic loss, which gives the lower limit of dielectric loss. In addition, As the frequency exceeds 10^{11} Hz, the extrinsic polarization will disappear from the response. Therefore, the mechanism of intrinsic loss can be explored by infrared reflection spectrum [33–35]. At present, more and more researchers use infrared reflectance spectroscopy to extrapolate the intrinsic loss of the microwave frequency band. Based on the Fresnel formula, the correlation between the reflectivity and the complex dielectric constant obeys [36]:

$$R(\omega) = \left|\frac{1-\sqrt{\varepsilon^*(\omega)}}{1+\sqrt{\varepsilon^*(\omega)}}\right|^2 \tag{5}$$

The Drude-Lorentz harmonic oscillator model is used to fit the FIR reflectivity spectrum, which is described by the following formula [37]:

$$\varepsilon^* = \varepsilon'(\omega) - i\varepsilon''(\omega) = \varepsilon_\infty + \sum_{j=1}^{n} \frac{\omega_{pj}^2}{\omega_{oj}^2 + \omega^2 + i\omega\gamma_j} \tag{6}$$

$\varepsilon'(\omega)$ and $\tan\delta$ are also obtained by extrapolating the frequency to the microwave range, and the formulas are as follows [38]:

$$\varepsilon'(w) = \varepsilon_\infty + \sum_{j=1}^{n} \Delta\varepsilon_j = \varepsilon_\infty + \sum_{j=1}^{n} \frac{w_{pj}^2}{w_{oj}^2} \tag{7}$$

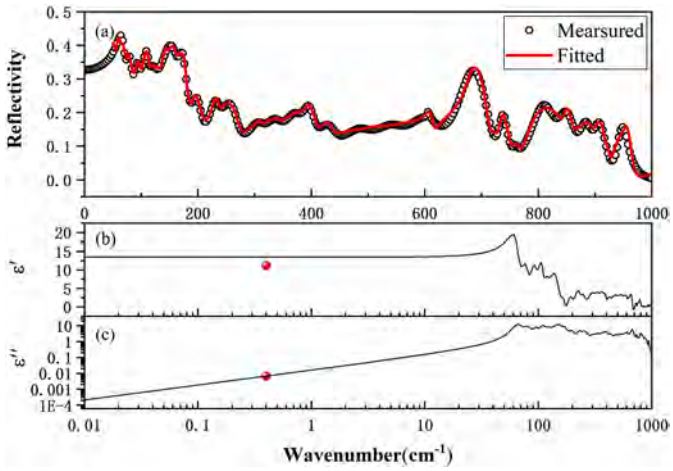

Fig. 6. (a) Experimental and fit infrared reflectivity spectra of $BaMnV_2O_7$ ceramics; (b) The real parts ε'(ω) and (c) the imaginary parts ε''(ω) of relative permittivity after fitting.

Table 3
Phonon parameters of $BaMnV_2O_7$ ceramic after fitting.

Mode	ω_{oj}	ω_{pj}	γ_j	$\Delta\varepsilon_j$	$\Delta\varepsilon_j/\varepsilon_j$(%)
1	66.39	100.33	13.91	2.28	16.94
2	80.29	71.65	10.81	0.80	5.91
3	95.41	68.77	11.08	0.52	3.85
4	109.76	90.08	11.14	0.67	5.00
5	122.43	90.39	18.43	0.55	4.04
6	150.42	235.52	34.75	2.45	18.18
7	170.56	96.57	14.91	0.32	2.38
8	197.82	110.52	22.60	0.31	2.32
9	231.11	111.31	21.02	0.23	1.72
10	256.33	182.31	38.32	0.51	3.75
11	307.36	132.56	37.48	0.19	1.38
12	337.64	148.74	38.40	0.19	1.44
13	371.65	175.77	38.72	0.22	1.66
14	395.28	154.43	25.02	0.15	1.13
15	430.01	172.02	41.06	0.16	1.19
16	487.01	241.70	73.48	0.25	1.83
17	542.99	246.05	70.58	0.21	1.52
18	600.82	324.43	72.74	0.29	2.16
19	606.40	40.03	5.28	0.00	0.03
20	673.39	403.17	47.16	0.36	2.66
21	734.88	137.92	17.66	0.04	0.26
22	759.63	51.07	10.82	0.00	0.03
23	800.11	326.41	47.57	0.17	1.23
24	842.35	192.17	38.55	0.05	0.39
25	878.03	146.06	28.53	0.03	0.21
26	901.94	115.10	24.64	0.02	0.12
27	940.62	123.76	19.75	0.02	0.13

($\varepsilon\infty = 2.5$, $\tan\delta = 3.8671 \times 10^{-4}$).

$$\varepsilon''(w) = \sum_{j=1}^{n} \frac{y_j \omega_{pj}^2}{\omega_{oj}^4} \omega \tag{8}$$

$$\tan\delta(\omega) = \frac{\varepsilon''(\omega)}{\varepsilon'(\omega)} = \omega \sum_{j=1}^{n} \frac{\Delta\varepsilon_j \gamma_j}{\omega_{oj}^2(\varepsilon_\infty + \sum_{j=1}^{n}\Delta\varepsilon_j)} \tag{9}$$

where $\varepsilon'(\omega)$ is the real part and $\varepsilon''(\omega)$ is the imaginary part of the complex relative permittivity. ε_∞ is the dielectric constant caused by the interaction of electron polarization at optical frequencies. ω_{oj},ω_{pj} and γ_j are the three dispersion parameters of the jth Lorentz oscillator: the plasma frequency, the transverse frequency and the damping factor. n is the number of polar phonon modes.

Fig. 6(a) shows the measured spectrum and the fitted curve with 27 models, and the phonon parameters of each model from the fitted curve are listed in Table 3. Fig. 6(b)(c) exhibit the real and imaginary parts of the complex permittivity. As seen from Table 3, the permittivity at the optical frequency is 2.5, and the permittivity extrapolated to the microwave frequency band through fitting is 13.48. The vibration modes below 400 cm^{-1} made major contributions to the relative permittivity (69.7%). The dielectric loss after fitting is almost the same as the measured value, so the fitted value is slightly higher than the measured dielectric constant, which may because of the existence of pores. And the dielectric loss is not much different from the measured value, it is concluded that the polarization of $BaMnV_2O_7$ ceramics in the microwave region is due to the influence of phonon absorption.

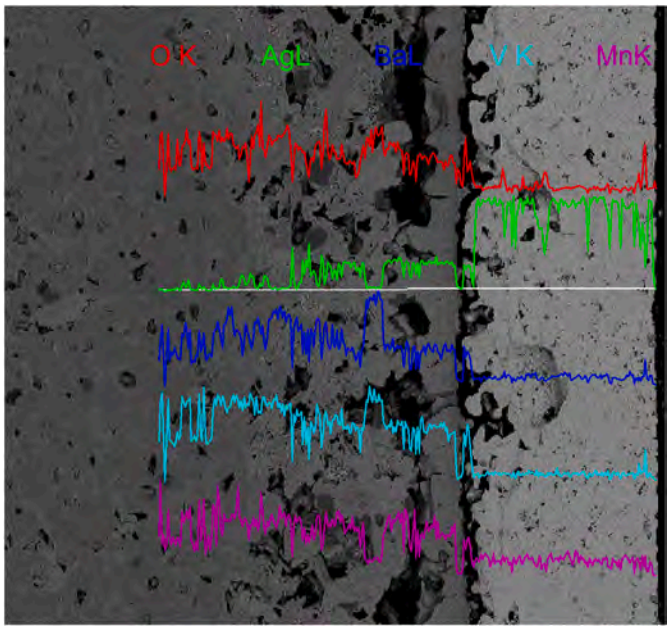

Fig. 7. SEM-EDS images and EDS analysis of cross section of $BaMnV_2O_7$ ceramic pellets co-fired with silver electrode at 830 °C/2h in air.

To verify the chemical compatibility between the $BaMnV_2O_7$ ceramic and Ag electrode, $BaMnV_2O_7$ brushed with Ag slurry was co-fired at 800 °C. Fig. 7 shows the SEM-EDS pattern of the $BaMnV_2O_7$ ceramic with silver. There was an obvious boundary between the $BaMnV_2O_7$ ceramic and silver electrode, which illustrated that it was stable between the $BaMnV_2O_7$ ceramic and silver during the sintering process. Moreover, according to the SEM-EDS analysis, silver was not detected in the interior of the ceramic. Thus, the SEM-EDS analysis suggested that $BaMnV_2O_7$ possessed good chemical compatibility with silver.

4. Conclusions

A $BaMnV_2O_7$ ceramic was synthetized by a solid-state reaction technique as a novel low-fired ceramic. XRD and TEM analyses confirmed that $BaMnV_2O_7$ crystallized in a monoclinic structure with a P21/n space group. SEM micrographs showed the surface morphology at different sintering temperatures, and a high density was obtained at 850 °C. In addition, the variation in the τ_f value was affected by the bond valence of V-O. Furthermore, fitting analysis of the infrared reflectivity spectra was conducted to investigate the major contributions to the intrinsic dielectric properties. The $BaMnV_2O_7$ ceramic sintered at 850 °C exhibited the optimum dielectric properties: $\varepsilon_r = 11.17$, $Q \times f = 20040$ GHz and $\tau_f = -48.2$ ppm/°C, and pores played a significant role in the dielectric performance of the samples. The SEM-EDS images exhibited good chemical stability of the $BaMnV_2O_7$ ceramic with a silver electrode.

Declaration of competing interest

The authors declare that they have no known competing financial interests or personal relationships that could have appeared to influence the work reported in this paper.

References

[1] D. Zhou, L.X. Pang, D.W. Wang, C. Li, B.B. Jin, I.M. Reaney, High permittivity and low loss microwave dielectrics suitable for 5G resonators and low temperature co-fired ceramic architecture, J. Mater. Chem. C 5 (2017) 10094–10098.
[2] C. Yin, C. Li, G. Yang, L. Fang, Y. Yuan, L. Shu, J. Khaliq, $NaCa_4V_5O_{17}$: a low-firing microwave dielectric ceramic with low permittivity and chemical compatibility with silver for LTCC applications, J. Eur. Ceram. Soc. 40 (2020) 386–390.
[3] H.-C. Huang, Y. Wang, X. Jian, Influence Analysis of ZrO_2 Ceramic for Cellular Phones on 5G mm-Wave Antenna Performance, 2018 IEEE Asia-Pacific Conference on Antennas and Propagation (APCAP), IEEE, 2018, pp. 420–424.
[4] Mailadil T. Sebastian, Rick Ubic, Heli Jantunen (Eds.), Microwave Materials and Applications, John Wiley & Sons, 2017.
[5] W. Lei, Z.Y. Zou, Z.H. Chen, B. Ullah, A. Zeb, X.K. Lan, W.Z. Lu, G.F. Fan, X. H. Wang, X.C. Wang, Controllable τf value of barium silicate microwave dielectric ceramics with different Ba/Si ratios, J. Am. Ceram. Soc. 101 (2018) 25–30.
[6] G.h. Chen, J.c. Di, H.r. Xu, M.h. Jiang, C.l. Yuan, Microwave dielectric properties of $Ca_4La_2Ti_{5-x}(Mg_{1/3}Nb_{2/3})_xO_{17}$ ceramics, J. Am. Ceram. Soc. 95 (2012) 1394–1397.
[7] H. Yang, S. Zhang, H. Yang, et al., Usage of P–V–L bond theory in studying the structural/property regulation of microwave dielectric ceramics: a review, Inorg. Chem. Front. 7 (23) (2020) 4711–4753.
[8] J. Raynaud, V. Pateloup, M. Bernard, D. Gourdonnaud, D. Passerieux, D. Cros, V. Madrangeas, T. Chartier, Hybridization of additive manufacturing processes to build ceramic/metal parts: example of LTCC, J. Eur. Ceram. Soc. 40 (2020) 759–767.
[9] D. Zhou, C.A. Randall, L.X. Pang, H. Wang, J. Guo, G.Q. Zhang, X.G. Wu, L. Shui, X. Yao, Microwave dielectric properties of Li2WO4 ceramic with ultra-low sintering temperature, J. Am. Ceram. Soc. 94 (2011) 348–350.
[10] M.T. Sebastian, H. Jantunen, Low loss dielectric materials for LTCC applications: a review, Int. Mater. Rev. 53 (2008) 57–90.
[11] M.T. Sebastian, H. Wang, H. Jantunen, Low temperature co-fired ceramics with ultra-low sintering temperature: a review, Curr. Opin. Solid State Mater. Sci. 20 (2016) 151–170.
[12] D. Zhou, L.-X. Pang, D.-W. Wang, I.M. Reaney, $BiVO_4$ based high k microwave dielectric materials: a review, J. Mater. Chem. C 6 (2018) 9290–9313.
[13] X. Chen, H. Li, P. Zhang, H. Hu, Y. Tao, G. Li, $SrZnV_2O_7$: a low-firing microwave dielectric ceramic with high-quality factor, J. Am. Ceram. Soc. (2021) 1–10.
[14] D. Zhou, D. Guo, W.-B. Li, L.-X. Pang, X. Yao, D.-W. Wang, I.M. Reaney, Novel temperature stable high-ε r microwave dielectrics in the Bi_2O_3–TiO_2–V_2O_5 system, J. Mater. Chem. C 4 (2016) 5357–5362.
[15] L. Fang, H. Guo, W. Fang, Z. Wei, C. Li, $BaTa_2V_2O_{11}$: a novel low fired microwave dielectric ceramic, J. Eur. Ceram. Soc. 35 (2015) 3765–3770.
[16] C. Su, L. Fang, Z. Wei, X. Kuang, H. Zhang, $LiCa_3ZnV_3O_{12}$: a novel low-firing, high Q microwave dielectric ceramic, Ceram. Int. 40 (2014) 5015–5018.
[17] M.R. Joung, J.S. Kim, M.E. Song, S. Nahm, J.H. Paik, Formation process and microwave dielectric properties of the $R_2V_2O_7$ (R= Ba, Sr, and Ca) ceramics, J. Am. Ceram. Soc. 92 (2009) 3092–3094.
[18] X.W. Jiang, C.C. Li, C.X. Su, Z.H. Wei, L. Fang, Low temperature firing and microwave dielectric properties of $BaCaV_2O_7$ ceramics, Ceram. Int. 41 (2015) 5172–5176.
[19] L. Fang, Z. Wei, C. Su, F. Xiang, H. Zhang, Novel low-firing microwave dielectric ceramics: $BaMV_2O_7$ (M=Mg, Zn), Ceram. Int. 40 (2014) 16835–16839.
[20] B.H. Toby, EXPGUI, a graphical user interface for GSAS, J. Appl. Crystallogr. 34 (2001) 210–213.
[21] S. Ramarao, V. Murthy, Structural, Raman spectroscopic and microwave dielectric studies on $Ni_{1-x}(Zn_{1/2}Zr_{1/2})_xW_{1-x}Nb_xO_4$ ceramic compounds with wolframite structure, Dalton Trans. 44 (2015) 2311–2324.
[22] S.J. Penn, N.M. Alford, A. Templeton, X. Wang, M. Xu, M. Reece, K. Schrapel, Effect of porosity and grain size on the microwave dielectric properties of sintered alumina, J. Am. Ceram. Soc. 80 (1997) 1885–1888.
[23] X. Chen, H. Li, P. Zhang, H. Hu, G. Chen, G. Li, A low-permittivity microwave dielectric ceramic $BaZnP_2O_7$ and its performance modification, J. Am. Ceram. Soc. (2021) 1–10.
[24] E.S. Kim, B.S. Chun, R. Freer, R.J. Cernik, Effects of packing fraction and bond valence on microwave dielectric properties of $A^{2+}B^{6+}O_4$(A^{2+}: Ca, Pb, Ba; B^{6+}: Mo, W) ceramics, J. Eur. Ceram. Soc. 30 (2010) 1731–1736.
[25] R.D. Shannon, Revised effective ionic radii and systematic studies of interatomic distances in halides and chalcogenides, Acta Crystallogr. Sect. A Cryst. Phys. Diffr. Theor. Gen. Crystallogr. 32 (1976) 751–767.
[26] Y. Wang, R. Zuo, A novel low-temperature fired microwave dielectric ceramic $BaMg_2V_2O_8$ with ultra-low loss, J. Eur. Ceram. Soc. 36 (2016) 247–251.
[27] M.C. Biesinger, L.W. Lau, A.R. Gerson, R.S.C. Smart, Resolving surface chemical states in XPS analysis of first row transition metals, oxides and hydroxides: Sc, Ti, V, Cu and Zn, Appl. Surf. Sci. 257 (2010) 887–898.
[28] Y. Zhang, H. Wu, Crystal structure and microwave dielectric properties of $La_2(Zr_{1-x}Ti_x)_3(MoO_4)_9$($0 \leq x \leq 0.1$) ceramics, J. Am. Ceram. Soc. 102 (2019) 4092–4102.
[29] H. Lim, Y.-J. Oh, Low-temperature sintered $Bi_{1-x}SmxNbO_4$ microwave dielectrics, J. Eur. Ceram. Soc. 40 (2020) 1191–1197.
[30] H.S. Park, K.H. Yoon, E.S. Kim, Relationship between the bond valence and the temperature coefficient of the resonant frequency in the complex perovskite $(Pb_{1-x}Ca_x)[Fe_{0.5}(Nb_{1-y}Ta_y)_{0.5}]O_3$, J. Am. Ceram. Soc. 84 (2001) 99–103.
[31] K.H. Yoon, W.S. Kim, E.S. Kim, Dependence of the octahedral bond valence on microwave dielectric properties of $Ca_{1-x}Sm_{2x/3}TiO_3$ ceramics, Mater. Sci. Eng., B 99 (2003) 112–115.
[32] N. Brese, M. O'keeffe, Bond-valence parameters for solids, Acta Crystallogr. Sect. B Struct. Sci. 47 (1991) 192–197.
[33] P.Y. Han, M. Tani, M. Usami, et al., A direct comparison between terahertz time-domain spectroscopy and far-infrared Fourier transform spectroscopy, J. Appl. Phys. 89 (2001) 2357–2359.
[34] K. Wakino, M. Murata, H. Tamura, Far infrared reflection spectra of $Ba(Zn,Ta)O_3$-$BaZrO_3$ dielectric resonator material, J. Am. Ceram. Soc. 69 (1) (1986) 34–37.
[35] H. Yang, S. Zhang, H. Yang, et al., Vibrational spectroscopic and crystal chemical analyses of double perovskite Y_2MgTiO_6 microwave dielectric ceramics, J. Am. Ceram. Soc. 103 (2) (2020) 1121–1130.
[36] K. Fukuda, R. Kitoh, I. Awai, Far-infrared reflection spectra of dielectric ceramics for microwave applications, J. Am. Ceram. Soc. 77 (1) (1994) 149–154.
[37] J. Guo, D. Zhou, Y. Li, T. Shao, Z.M. Qi, B.B. Jin, H. Wang, Structure-property relationships of novel microwave dielectric ceramics with low sintering temperatures: $(Na_{(0.5x)}Bi_{(0.5x)}Ca_{(1-x)})MoO_{(4)}$, Dalton Trans. 43 (2014) 11888–11896.
[38] Y. Zhao, P. Zhang, Effects of lanthanides on structural and dielectric properties of $NdNbO_4$-$LnNbO_4$ ceramics, Ceram. Int. 44 (2018) 1935–1941.